Cluster spin glass state in $Ba_3Sb_{1+x}Co_{2-x}O_{9-\delta}$: Cation disorder and mixed-valence Co dimers

Anzar Ali [1,*,†] Guratinder Kaur,[1,2,*] Lukas Keller [3] and Masahiko Isobe[1,‡]

[1]*Max Planck Institute for Solid State Research, Heisenbergstraße 1, D-70569 Stuttgart, Germany*

[2]*School of Physics and Astronomy, The University of Edinburgh, Edinburgh EH9 3JZ, United Kingdom*

[3]*Laboratory for Neutron Scattering and Imaging, Paul Scherrer Institute, CH-5232 Villigen, Switzerland*

(Received 10 March 2025; accepted 23 June 2025; published 7 July 2025)

We investigate the structural, magnetic, and thermodynamic properties of $Ba_3Sb_{1+x}Co_{2-x}O_{9-\delta}$ ($x = 0.04$, $\delta = 0.54$), a hexagonal perovskite featuring face-sharing CoO_6 octahedra that form Co dimers. DC and AC magnetization measurements reveal a frequency-dependent spin-freezing transition consistent with glassy dynamics. AC susceptibility fits best to the Vogel-Fulcher model, indicating collective freezing of interacting spin clusters. Isothermal magnetization follows the Langevin function, suggesting finite-sized magnetic clusters rather than isolated paramagnetic moments. Nonequilibrium dynamics, evidenced by thermoremanent magnetization and memory effects, further support a spin-glass-like state. Heat capacity shows no sharp anomalies, and neutron powder diffraction confirms the absence of magnetic Bragg peaks down to 1.5 K, ruling out long-range magnetic order. Rietveld refinement reveals significant Co/Sb intersite disorder (∼30%) and oxygen nonstoichiometry, introducing exchange randomness and frustration that drive the spin-glass-like behavior. Electrical resistivity exhibits Arrhenius-type temperature dependence with an activation energy of 0.173 eV, consistent with semiconducting behavior. Temperature-dependent x-ray diffraction shows no structural phase transitions, confirming that the spin-glass-like state is not lattice driven. Our results establish $Ba_3Sb_{1+x}Co_{2-x}O_{9-\delta}$ as a cluster spin-glass candidate, where Co dimers, disorder, and geometric frustration prevent long-range order, leading to slow spin dynamics. These findings highlight the role of cation disorder and oxygen vacancies in stabilizing unconventional magnetic states in cobalt-based hexagonal perovskites.

DOI: 10.1103/k7mm-g2zc

I. INTRODUCTION

The study of geometrically frustrated and disordered magnetic systems remains a focal point in condensed matter physics, primarily due to their capacity to host unconventional magnetic ground states [1–3]. Among these, spin glasses, materials characterized by frozen, disordered spin configurations, exhibit rich physics driven by competing exchange interactions and disorder-induced frustration [4,5]. In transition-metal oxides, the interplay between local disorder, mixed-valence states, and geometric frustration give rise to complex magnetic behaviors, covering spin-glass states to reentrant magnetic phases [6–8].

Hexagonal perovskites of the form $A_4BB'_3O_{12}$ and $A_3BB'_2O_9$ have emerged as versatile platforms for exploring such exotic magnetism [9]. These materials accommodate diverse structural motifs, including face-sharing $B'O_6$ octahedral trimers or dimers, fostering strong intraunit magnetic coupling that competes with weaker interunit interactions. This competition, further modulated by cation disorder and charge fluctuations, can profoundly influence the magnetic ground state. For example, trimer-based compounds such as $Ba_4NbIr_3O_{12}$ [10], $Ba_4NbRh_3O_{12}$ [11], and $Ba_4TaMn_3O_{12}$ [12], along with dimer-based systems like $Ba_3NiSb_2O_9$ [13], $Ba_3CuSb_2O_9$ [14], and $Ba_3FeRu_2O_9$ [15], display varying degrees of magnetic frustration and disorder, leading to behaviors that span from spin-glass states to potential quantum-disordered phases.

Disorder-induced quantum spin-liquid-like states have been proposed in several frustrated magnetic systems where magnetic and nonmagnetic ions either substitute each other or share the same crystallographic site. Examples include $Ho_2Ti_2O_7$ [16], $Pr_2Zr_2O_7$ [17], $Ba_3CuSb_2O_9$ [18], and Y_2CuTiO_6 [19]. In such cases, disorder can introduce long-range quantum entanglement, stabilizing diverse ground states such as Coulombic spin liquids, Mott glass phases, or conventional glassy states, depending on its extent [16]. In Y_2CuTiO_6, magnetic Cu^{2+} ($S = 1/2$) and nonmagnetic Ti^{4+} randomly share the same crystallographic site in a 50:50 ratio, forming a triangular lattice. Despite significant site dilution, no long-range order or spin freezing is observed down to 50 mK, indicating a disorder-driven cooperative paramagnetic state. Similarly, in $Ba_3CuSb_2O_9$, 50% site sharing of Cu^{2+} with Sb^{5+} leads to spin-orbital liquid-like behavior [18].

*These authors contributed equally to this work.

†Contact author: a.ali@fkf.mpg.de

‡Contact author: m.isobe@fkf.mpg.de

Published by the American Physical Society under the terms of the Creative Commons Attribution 4.0 International license. Further distribution of this work must maintain attribution to the author(s) and the published article's title, journal citation, and DOI. Open access publication funded by Max Planck Society.

$Sr_3CuSb_2O_9$, with 33% Cu and 67% Sb site disorder, also shows spin-liquid-like behavior down to 65 mK [20].

Controlled chemical substitution has proven an effective strategy to tune quantum states in frustrated magnets. For instance, substituting Ru^{3+} with nonmagnetic Ir^{3+} in the Kitaev magnet α-$Ru_{1-x}Ir_xCl_3$ introduces quenched disorder that stabilizes a spin-liquid-like state [21]. Such substitutions typically introduce both structural disorder—through random occupancy of crystallographic sites—and magnetic disorder—through disruption of magnetic exchange pathways. Intersite cation disorder is also known to strongly influence magnetic ground states, often promoting spin-glass behavior in frustrated magnets. In $MnSb_2Se_4$, ∼26% antisite disorder between Mn and Sb sites leads to long-range antiferromagnetic order ($T_N = 22.5$ K) with type-II multiferroicity, whereas increasing the disorder to ∼40% transforms the system into a cluster spin glass with significantly modified magnetic and transport properties [22]. A similar scenario occurs in the hexagonal perovskite $Ba_3Co[Co_{0.25}Ru_{0.75}]_2O_9$, where mixed-valence Co and Ru ions occupy the face-sharing octahedral sites, and the resulting cation disorder and charge transfer effects stabilize a spin-glass state with a giant exchange bias [23].

$Ba_3Sb_{1+x}Co_{2-x}O_{9-\delta}$, the focus of this study, belongs to the family of 6H-hexagonal perovskites and features CoO_6 octahedral dimers arranged in a triangular network. Unlike well-ordered dimer systems that often stabilize quantum spin-singlet states or develop long-range magnetic order, $Ba_3Sb_{1+x}Co_{2-x}O_{9-\delta}$ exhibits a cluster spin-glass ground state—an outcome of pronounced magnetic frustration and substantial cation disorder. This disorder encompasses both structural contributions, arising from Co/Sb intersite mixing (∼30%), and magnetic disruptions, due to broken dimer connectivity and randomized exchange interactions. These perturbations destabilize the uniform magnetic exchange network, giving rise to spatially inhomogeneous spin environments and resulting in a frozen, disordered magnetic state.

In this context, dimer-based hexagonal perovskites with the general formula $A_3MM'_2O_9$ provide an ideal platform to investigate disorder- and frustration-driven glassy magnetism, as they are inherently susceptible to M/M' intersite mixing. In $Ba_3Sb_{1+x}Co_{2-x}O_{9-\delta}$, the face-sharing CoO_6 dimers promote strong intradimer antiferromagnetic or ferromagnetic correlations via short Co-Co distances. However, the presence of intersite disorder and potential mixed valency fragments the magnetic lattice, suppressing coherent long-range correlations. These conditions favor the formation of weakly coupled spin clusters embedded in a disordered matrix—an ideal setting for the emergence of a cluster spin-glass state. Thus, systems like $Ba_3Sb_{1+x}Co_{2-x}O_{9-\delta}$, by virtue of their structural topology and chemical instability, are naturally predisposed to hosting unconventional frozen magnetic states, offering a fertile ground for exploring novel manifestations of frustration-induced glassy behavior.

Experimental data from DC and AC magnetic susceptibility measurements show a bifurcation between field-cooled and zero-field-cooled magnetization below ∼50 K, alongside frequency-dependent peaks in AC susceptibility, which is a hallmark of spin-glass behavior. Neutron diffraction confirms the absence of magnetic Bragg peaks down to 1.5 K, ruling out the possibility of conventional long-range order. Specific heat measurements reveal no sharp anomalies, consistent with a frozen, disordered magnetic state. Scaling analysis of the AC susceptibility supports a cluster spin-glass scenario, where weakly interacting ferromagnetic clusters remain dynamically frustrated.

Our findings highlight that the spin-glass state in $Ba_3Sb_{1+x}Co_{2-x}O_{9-\delta}$ results from the interplay of cation disorder, mixed-valence states, and competing magnetic interactions. Disruptions in the ideal face-sharing dimer network inhibit singlet formation and long-range order, stabilizing a glassy state composed of frozen spin clusters. This study deepens our understanding of disorder-driven magnetism in low-dimensional oxides and underscores the complex relationship between structural disorder and magnetic behavior in transition-metal perovskites.

II. EXPERIMENTAL DETAILS

A. Sample preparation

Polycrystalline samples of $Ba_3Sb_{1+x}Co_{2-x}O_{9-\delta}$ were synthesized using the conventional solid-state reaction method. High-purity $BaCO_3$ (99.997%, Thermo Scientific), Sb_2O_5 (99.998%, Thermo Scientific), and Co_3O_4 (99.9985%, Thermo Scientific) were used as starting materials. The precursors were weighed in stoichiometric ratios, thoroughly mixed in an agate mortar, and subjected to initial calcination at 900 °C for 12 hours. The resulting powders were then pressed into pellets and sintered in air at 1000 °C for 24 hours, followed by a subsequent annealing step at 1100 °C for another 24 hours, with multiple intermediate grindings and pelletization to ensure homogeneity.

B. X-ray and neutron diffraction measurements

Room-temperature x-ray diffraction (XRD) data for $Ba_3Sb_{1+x}Co_{2-x}O_{9-\delta}$ were collected on a Rigaku SmartLab diffractometer using monochromatic Cu-Kα radiation ($\lambda = 1.5406$ Å), with measurements spanning $10^\circ \leqslant 2\theta \leqslant 120^\circ$ at a step size of 0.02°. Temperature-dependent XRD studies were conducted at the Centre for Science at Extreme Conditions (CSEC, University of Edinburgh, UK) using an Oxford cryostat for the measurements ranging from 300 to 15 K.

Neutron powder diffraction (NPD) data were acquired at the DMC cold neutron diffractometer at SINQ, Paul Scherrer Institute (PSI, Switzerland). Measurements covered temperatures of 300, 80, 50, 30, 20, and 1.5 K, with an incident neutron wavelength of 2.454 Å and angular range $10^\circ \leqslant 2\theta \leqslant 120^\circ$ (step size 0.1°). The sample was loaded in a vanadium can and cooled using a helium cryostat, achieving a base temperature of 1.5 K.

Rietveld refinements of XRD and NPD data were performed using JANA2006 [24] to model crystal structures, site occupancies, and thermal parameters. Diffraction patterns were corrected for instrumental contributions and background before refinement.

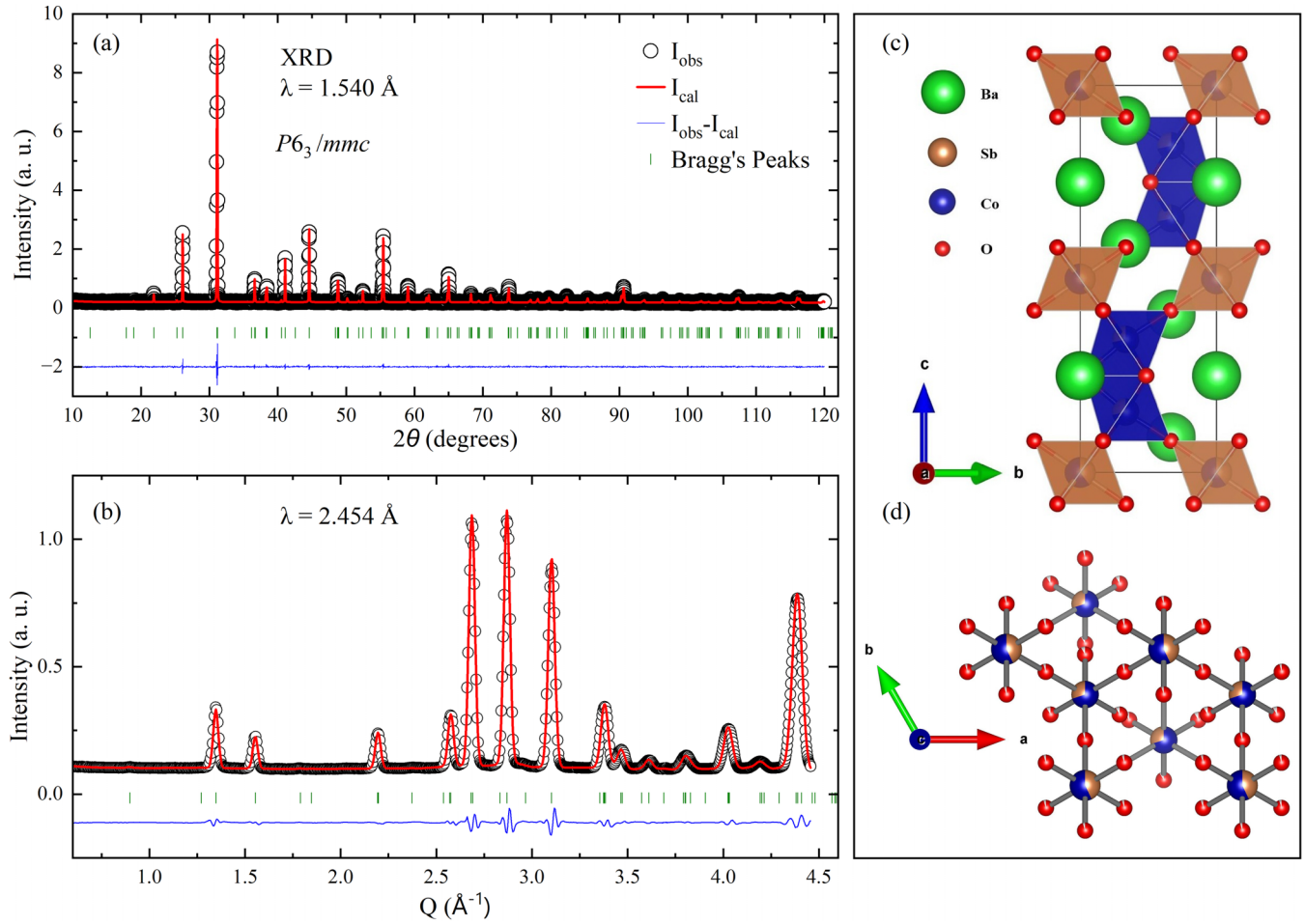


FIG. 1. (a) Rietveld refinement of the powder x-ray diffraction data collected at room temperature. (b) Rietveld refinement of the neutron powder diffraction data for $Ba_3Sb_{1+x}Co_{2-x}O_{9-\delta}$ at 300 K. (c) Refined crystal structure of $Ba_3Sb_{1+x}Co_{2-x}O_{9-\delta}$. (d) Co and Sb form a triangular lattice in the *ab* plane. The Co_2O_9 dimers, formed by face-sharing CoO_6 octahedra, are highlighted in blue along the *c* axis. The black open circles represent the observed diffraction pattern, the red solid line indicates the calculated fit, and the blue line at the bottom shows the difference between the observed and calculated intensities. The olive vertical markers denote the positions of allowed Bragg reflections.

C. Energy-dispersive x-ray spectroscopy

Energy-dispersive x-ray (EDX) spectra were acquired using a NORAN System 7 (NSS212E) detector integrated into a Tescan Vega (TS-5130MM) scanning electron microscope. Semiquantitative EDX analysis of the $Ba_3Sb_{1+x}Co_{2-x}O_{9-\delta}$ pellet yielded elemental ratios of Ba:Sb:Co = 3.00:1.05:2.10, confirming the expected stoichiometry within experimental uncertainty.

D. Magnetic, thermal, and electrical transport measurements

The temperature dependence of DC magnetic susceptibility was measured under zero-field-cooled (ZFC) and field-cooled (FC) conditions using a SQUID magnetometer (Quantum Design, MPMS-XL) in applied fields ranging from 50 Oe to 10 000 Oe over the temperature range of 1.8–300 K. Isothermal magnetization measurements were performed in magnetic fields sweeping from −70 kOe to +70 kOe. AC susceptibility was measured between 2 and 50 K with an AC magnetic field of 10 Oe amplitude and frequencies varying from 1 to 1000 Hz using the same SQUID magnetometer.

Specific heat capacity was measured using the thermal relaxation method in a Quantum Design PPMS over the temperature range of 1.8–200 K. The sintered pellet was affixed to a thin alumina platform with Apiezon N grease to ensure optimal thermal contact.

Electrical resistivity was measured on sintered rectangular pellets using a four-probe method in a Quantum Design PPMS over the temperature range of 120–300 K. Gold wires and silver epoxy were used for electrical contacts. The measured resistance was converted to resistivity based on the sample's dimensions.

III. RESULTS

A. Crystal structure

1. X-ray diffraction

To determine the crystal structure and assess phase purity, powder x-ray diffraction measurements were performed on $Ba_3Sb_{1+x}Co_{2-x}O_{9-\delta}$ at room temperature. Figure 1(a) displays the XRD pattern along with the Rietveld refinement.

The results confirm that $Ba_3Sb_{1+x}Co_{2-x}O_{9-\delta}$ crystallizes in a hexagonal perovskite structure with space group $P6_3/mmc$ (No. 194), consistent with structurally related compounds such as $Ba_3CoSb_2O_9$ and $Ba_3NiSb_2O_9$ [25–27]. The refined lattice parameters are $a = 5.7284(2)$ Å and $c = 14.0725(7)$ Å, yielding a goodness of fit of 1.03, a profile reliability factor $R_p = 5.31\%$, and a weighted profile factor $wR_p = 6.68\%$.

The refined crystal structure is illustrated in Figs. 1(c) and 1(d). It features Co_2O_9 dimers formed by face-sharing CoO_6 octahedra—structural motifs central to the material's magnetic behavior. These dimers are linked via corner-sharing SbO_6 octahedra, constructing a layered hexagonal framework. In the *ab* plane, Co and Sb ions generate triangular networks of partially disordered octahedra. The refined site occupancies reveal substantial Co/Sb intersite mixing (∼30%), indicating significant cation disorder that alters the local bonding environment and magnetic exchange pathways.

Earlier studies on $Ba_2Sb_xCo_{2-x}O_{6-\delta}$ [25] also reported a similar hexagonal structure with notable Sb/Co site disorder. In contrast, our work on $Ba_3Sb_{1+x}Co_{2-x}O_{9-\delta}$ provides a more comprehensive investigation of its thermodynamic and transport behavior, including heat capacity, AC susceptibility, and electrical resistivity. The observed spin-glass-like transition underscores the crucial role of cation disorder and possible mixed-valence states in disrupting long-range magnetic order, highlighting the complexity of magnetic interactions in this dimer-based system.

2. Neutron powder diffraction

To further investigate the structural and magnetic properties of $Ba_3Sb_{1+x}Co_{2-x}O_{9-\delta}$, neutron powder diffraction measurements were performed at 300, 80, 50, 30, 20, and 1.5 K. No additional magnetic Bragg reflections were observed at low temperatures compared to the 300 K pattern, confirming the absence of long-range magnetic ordering down to 1.5 K. Rietveld refinement of the 300 K NPD data [Fig. 1(b)] yielded precise atomic positions, site occupancies, and insights into structural disorder.

To explore the presence of short-range magnetic correlations, we analyzed the low-Q region of the diffraction patterns at various temperatures. No temperature-dependent diffuse magnetic scattering features were detected, indicating an absence of significant short-range magnetic order. This suggests that any spin correlations within magnetic clusters are confined to very short length scales—too limited to generate observable diffuse features. A similar lack of diffuse scattering has been reported in related cluster spin-glass systems such as $CaMnFeTaO_6$ [28], where the extremely short correlation length renders magnetic scattering indistinguishable from the background.

The refined structural parameters (Table I) reveal two key features: (i) pronounced intersite mixing (30%) between Sb and Co at the 4*f* Wyckoff position, and (ii) a notable oxygen deficiency ($\delta = 0.54$). The cation disorder—arising from the statistical distribution of Co and Sb ions over shared crystallographic sites—generates random local environments, introducing frustration into the magnetic exchange interactions and likely stabilizing the observed spin-glass state. Each unit cell of $Ba_3Sb_{1+x}Co_{2-x}O_{9-\delta}$ contains two crystallographically equivalent Co-Co dimers formed by face-sharing CoO_6 octahedra, with an intradimer Co-Co distance of approximately 2.64 Å and a shortest interdimer Co-Co distance of about 5.73 Å.

TABLE I. Refined structural parameters for $Ba_3Sb_{1+x}Co_{2-x}O_{9-\delta}$ ($x = 0.04$, $\delta = 0.54$) at 300 K extracted from the Rietveld refinement of neutron powder diffraction data. Space group $P6_3/mmc$, No. 194, $a = 5.7289(2)$ Å, $c = 14.0800(12)$ Å, $R_p = 2.05\%$, and $wR_p = 2.95\%$.

Atom	*x*	*y*	*z*	Occupancy	U_{iso}	Site
Ba1	0.0000	0.0000	0.2500	1.000	0.001(1)	2*b*
Ba2	0.3333	0.6667	0.0916(5)	1.000	0.008(1)	4*f*
Co1	0.3333	0.6667	0.84385(6)	0.696(4)	0.025(2)	4*f*
Sb1	0.3333	0.6667	0.84385(6)	0.304(4)	0.025(2)	4*f*
Sb2	0.0000	0.0000	0.0000	0.433(2)	0.001(1)	2*a*
Co2	0.0000	0.0000	0.0000	0.567(2)	0.001(1)	2*a*
O1	0.5197(6)	1.0395(13)	0.25000	0.914(1)	0.010(1)	6*h*
O2	0.8338(4)	1.6677(8)	0.0818(1)	0.952(3)	0.005(2)	12*k*

Local distortions of the CoO_6 octahedra were quantified through bond-angle analysis. For the Co1 site (4*f*), bond angles deviate markedly from the ideal 90°, with representative values of 85.1°, 92.3°, and 88.7°. Similar deviations are found at the Co2 site (2*a*), with angles of 84.9°, 93.1°, and 89.5°. Assuming an oxidation state of +5 for Sb, the refined stoichiometry corresponds to an average Co oxidation state of +2.9, consistent with a mixed-valent population of roughly 10% Co^{2+} and 90% Co^{3+}. This mixed-valence character, coupled with octahedral distortions, generates a locally heterogeneous electronic environment that modulates magnetic exchange. Bond valence sum (BVS) calculations (see Table IV, Appendix B) support this oxidation state distribution.

Oxygen vacancies were refined at both O1 and O2 sites, with a stronger deficiency at the O1 site [$o(O1) = 0.914$ vs $o(O2) = 0.952$]. These vacancies predominantly reside within the BaO_3 layers that bridge the face-sharing CoO_6 dimers, a feature common in 6H-hexagonal perovskites such as Ba_2ScAlO_5 [29] and $BaFeO_{2.73}$ [30]. The resulting reduction in electrostatic screening between neighboring Co ions can lead to Co-Co distance contraction, as observed in oxygen-deficient $BaTiO_{3-y}$ [31]. Furthermore, the uneven distribution of vacancies promotes the formation of undercoordinated CoO_4 tetrahedral motifs, reducing the connectivity of face-sharing octahedra. This structural reconfiguration mirrors features seen in hexagonal analogs of brownmillerite phases [32], where altered coordination and metal-metal separations contribute to enhanced magnetic frustration via disrupted superexchange pathways.

B. DC magnetization

Magnetization and susceptibility measurements were performed to investigate the magnetic behavior of $Ba_3Sb_{1+x}Co_{2-x}O_{9-\delta}$. Figure 2(a) displays the temperature-dependent magnetic susceptibility measured under zero-field-cooled (ZFC) and field-cooled (FC) conditions, along with the inverse susceptibility, all recorded under an

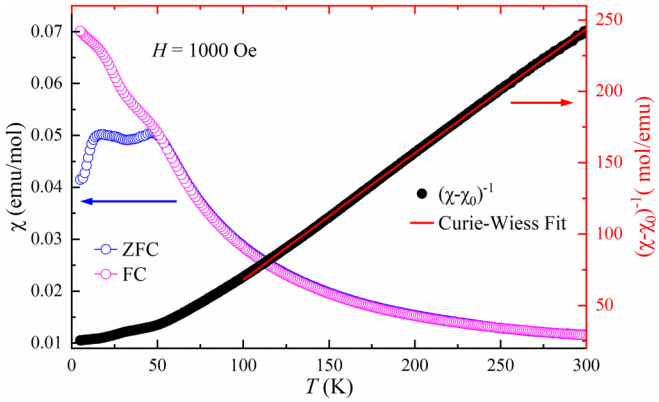


FIG. 2. Temperature dependence of magnetic susceptibility (ZFC-FC) (left y axis) and inverse susceptibility with Curie-Weiss fit (right y axis) for $Ba_3Sb_{1+x}Co_{2-x}O_{9-\delta}$ at an applied field of 1000 Oe. The red solid line represents the CW fit in the range 100–300 K.

applied magnetic field of 1000 Oe over the temperature range 2–300 K. The left y axis corresponds to the ZFC-FC susceptibility, while the right y axis shows the inverse susceptibility. A clear bifurcation between the ZFC and FC curves emerges below approximately 50 K, signaling magnetic irreversibility that may originate from magnetic frustration or a spin-glassy ground state. In the high-temperature region (100–300 K), the susceptibility follows a modified Curie-Weiss (CW) behavior:

$$\chi(T) = \chi_0 + \frac{C}{T-\theta}, \tag{1}$$

where χ_0 is the temperature-independent susceptibility, C is the Curie constant, and θ is the Curie-Weiss temperature. The effective magnetic moment is determined using $\mu_{\text{eff}} = \sqrt{3k_BC/N_A}$, where N_A is Avogadro's constant and k_B is the Boltzmann constant [33]. The fit yields an effective moment of $\mu_{\text{eff}} = 2.96\ \mu_B$.

To interpret this effective moment, we consider the formal oxidation states based on stoichiometry. Assuming Ba^{2+}, Sb^{5+}, and O^{2-}, the average oxidation state of Co is calculated as +2.9, suggesting a mixed-valence state with a possible distribution of 10% Co^{2+} and 90% Co^{3+}. To explore how different spin states influence the observed magnetic moment, we consider combinations of high-spin, intermediate-spin, and low-spin states for both Co^{2+} and Co^{3+}.

The calculated effective magnetic moments for these configurations are summarized in Table II. The theoretical effective moment for this mixed-valence system is calculated using

$$\mu_{\text{eff}}^{\text{theory}} = \sqrt{0.1\,\mu_{\text{eff}}(Co^{2+})^2 + 0.9\,\mu_{\text{eff}}(Co^{3+})^2}. \tag{2}$$

TABLE II. Calculated effective magnetic moments (μ_{eff}) for various spin-state combinations of Co^{2+} (10%) and Co^{3+} (90%).

Co^{2+} Spin State	Co^{3+} Spin State	μ_{eff} (μ_B)
High spin	High spin	4.81
High spin	Intermediate spin	2.95
High spin	Low spin	1.22
Low spin	High spin	4.68
Low spin	Intermediate spin	2.74
Low spin	Low spin	0.55

Although intermediate-spin Co^{3+} is less common, crystal field effects, local lattice distortions, and covalency can stabilize such states in certain cobalt oxides [34,35].

The experimentally observed $\mu_{\text{eff}} = 2.96\ \mu_B$ is closest to the scenario where Co^{2+} adopts a high-spin configuration ($\mu_{\text{eff}} = 3.88\ \mu_B$) and Co^{3+} is in an intermediate-spin state ($\mu_{\text{eff}} = 2.8\ \mu_B$). Using these values in Eq. (1), the resulting theoretical effective moment is $\mu_{\text{eff}}^{\text{theory}} \approx 2.95\ \mu_B$ [34–38], which is in close agreement with the experimental data.

This supports a mixed-valence state comprising Co^{2+} and Co^{3+}, consistent with an average oxidation state of +2.9. While this scenario is plausible, the stabilization of an intermediate-spin state for Co^{3+} remains speculative and warrants further spectroscopic or structural studies.

The mixed-valent state, combined with oxygen vacancies primarily located at the oxygen sites, likely plays a significant role in modifying local magnetic interactions and electronic properties [39,40]. Furthermore, the extracted Curie-Weiss temperature of $\theta \sim 21$ K is positive, indicative of dominant ferromagnetic interactions and suggesting that the magnetic behavior is primarily governed by interactions at the dimer level rather than between individual Co spins. In $Ba_3Sb_{1+x}Co_{2-x}O_{9-\delta}$, the face-sharing CoO_6 dimers likely host antiferromagnetic intradimer exchange interactions, facilitated by direct Co-Co orbital overlap. However, ferromagnetic correlations between these dimers within the triangular ab plane may arise via longer-range superexchange pathways through bridging oxygens or via polarizable Sb-O units. This combination of AFM intradimer and FM interdimer couplings can collectively yield a net positive Curie-Weiss temperature. A similar scenario has been discussed in the trimer-based system $Ba_4NbMn_3O_{12}$, where antiferromagnetic interactions dominate within Mn_3 clusters, but ferromagnetic coupling between clusters leads to overall positive θ [41].

A noteworthy feature is the positive value of $\chi_0 = 2.7 \times 10^{-3}$ emu/mol, which is suggestive of Van Vleck paramagnetism [33]. This observation is consistent with a scenario where local moments remain partially aligned even at elevated temperatures, likely due to remnant interactions within the Co dimers. Similar behavior has been observed in structurally related systems such as $Ba_4NbMn_3O_{12}$ [10], $Ba_4TaMn_3O_{12}$ [12], $Ba_4NbRu_3O_{12}$ [42], and $Ba_4Nb_{0.8}Ir_{3.2}O_{12}$ [43].

To further explore the magnetic behavior, isothermal magnetization (M vs H) measurements were conducted at 2, 25, and 50 K, as shown in Fig. 3. The magnetization curves show a gradual increase with applied field, exhibiting slight curvature at low fields and approaching linear behavior at higher fields. At 2 K, a weak hysteresis loop is observed, indicative of minor magnetic irreversibility. Notably, the magnetization does not saturate up to 70 kOe, reaching a maximum value of only $\sim 0.45\ \mu_B$ per formula unit. This is significantly lower than the expected theoretical saturation moment of $M_{\text{sat}} \sim 2.1\ \mu_B$ per formula unit for a mixed-valence Co^{2+} (high spin) and Co^{3+} (intermediate spin) scenario. The absence of sharp metamagnetic transitions or magnetization plateaus further suggests a

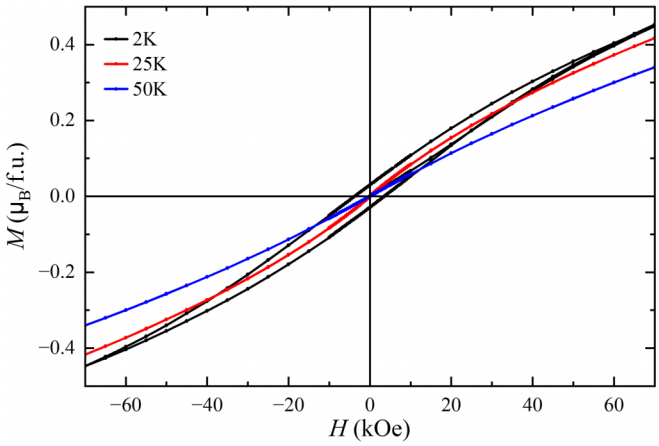


FIG. 3. Isothermal magnetization (M vs H) curves at different temperatures ($T = 2$, 25, and 50 K).

lack of long-range magnetic order, consistent with a magnetically frustrated state.

The strongly reduced magnetization and absence of saturation indicate the presence of persistent spin dynamics and frozen short-range correlations, characteristics often associated with spin-glass-like behavior. The weak hysteresis observed at 2 K further supports the presence of glassy magnetic dynamics. Such behavior typically arises from competing interactions, local disorder, and geometric frustration within the Co dimers, which collectively hinder the establishment of long-range magnetic order.

The coexistence of Co^{2+} and Co^{3+} in a mixed-valence state, along with possible oxygen vacancies and structural distortions, likely enhances the degree of magnetic frustration. These factors may promote collective spin freezing, similar to phenomena observed in related cobalt oxides [39,40,44].

C. Heat capacity

To further investigate the anomalous magnetic behavior observed in the susceptibility measurements, we performed heat capacity measurements on the same sample. Figure 4(a) presents the specific heat divided by temperature (C_p/T) between 2 and 200 K at 0 and 9 T. A broad feature is observed around 30 K, indicative of short-range magnetic correlations. Notably, applying a 9 T field suppresses this feature at lower temperatures, confirming its magnetic origin.

In insulating magnetic materials, the total heat capacity (C_p) consists of contributions from phononic (C_{ph}) and magnetic (C_{mag}) degrees of freedom. Ideally, these components can be separated by measuring a nonmagnetic structural analog; however, without such a reference compound, we employed a Debye-Einstein model [45,46] to approximate the lattice contribution. The phonon heat capacity was modeled using a combination of one Debye and one Einstein term, given by

$$C_{ph}(T) = f_D C_D(\theta_D, T) + g_E C_E(\theta_E, T), \tag{3}$$

where the Debye contribution, representing acoustic phonon modes, is expressed as

$$C_D(\theta_D, T) = 9nR\left(\frac{T}{\theta_D}\right)^3 \int_0^{\theta_D/T} \frac{x^4 e^x}{(e^x - 1)^2} dx, \tag{4}$$

with n being the number of atoms per formula unit, R the universal gas constant, θ_D the Debye temperature, and $x = \frac{\hbar\omega}{k_B T}$. The Einstein term, accounting for optical phonon modes, follows

$$C_E(\theta_E, T) = 3nR\left(\frac{\theta_E}{T}\right)^2 \frac{e^{\theta_E/T}}{(e^{\theta_E/T} - 1)^2}, \tag{5}$$

where θ_E is the Einstein temperature. Given that $Ba_3Sb_{1+x}Co_{2-x}O_{9-\delta}$ has 15 atoms per formula unit, the sum of f_D and g_E is constrained to 15, ensuring the model accounts for all lattice vibrations.

The best fit of C_p data between 50 and 200 K yields $\theta_D \approx 776$ K and $\theta_E \approx 190$ K, with $f_D \approx 9$ and $g_E \approx 6$ [magenta solid line in the inset of Fig. 4(a)]. Alternative models incorporating additional Einstein terms or a purely Debye-based fit yielded a poorer agreement, justifying our minimal one-Debye, one-Einstein model. By subtracting the fitted

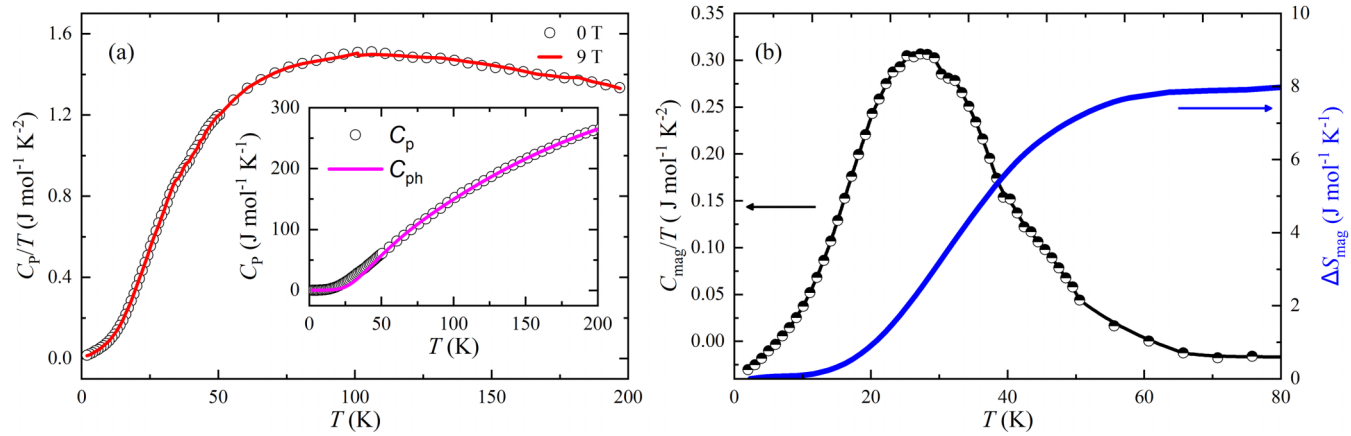


FIG. 4. Heat capacity (C_p) data analysis. (a) Temperature dependence of C_p/T measured at zero and 9 T between 2 and 200 K. The inset shows the total measured heat capacity (symbols) overlaid with the estimated phononic contribution at zero field (magenta line; see text). (b) Magnetic contribution to heat capacity ($C_p - C_{ph}$) divided by temperature (left y axis) and the evolution of the magnetic entropy, $\Delta S_{mag}(T)$ (right y axis).

phononic contribution from the measured C_p at zero field, we extract the magnetic contribution, C_{mag}, which is plotted in Fig. 4(b).

The temperature dependence of C_{mag}/T reveals a broad hump centered around 30 K, a hallmark of short-range spin correlations rather than a sharp λ-type anomaly associated with long-range magnetic ordering. This behavior is consistent with a spin-glass or cluster-glass state, where magnetic moments freeze gradually rather than undergoing a sharp phase transition. The suppression of this feature under a 9 T field further supports this interpretation, suggesting that applied fields destabilize frozen spin configurations.

Figure 4(b) also shows the evolution of the magnetic entropy (ΔS_{mag}) as a function of temperature (blue solid line). The total magnetic entropy change is obtained by integrating the magnetic heat capacity (C_{mag}) divided by temperature over the 2–80 K range:

$$\Delta S_{mag}(T) = \int_{2\,K}^{80\,K} \frac{C_{mag}}{T} dT. \tag{6}$$

This integration yields a total entropy change of $\Delta S_{mag} = 8.15\ J\ mol^{-1}\ K^{-1}$. For the mixed-valence state of Co^{2+} (high spin, $S = 3/2$) and Co^{3+} (intermediate spin, $S = 1$), the theoretical magnetic entropy is calculated as $\Delta S_{mag} = 0.1R\ln(4) + 0.9R\ln(3) \approx 9.38\ J\ mol^{-1}\ K^{-1}$. The observed entropy change is reasonably close to this theoretical value, with the slight deficit possibly arising from residual quantum fluctuations, partial spin freezing, or covalency effects that suppress the full recovery of spin entropy. Such behavior is often observed in frustrated systems and cluster spin glasses, where competing interactions and local structural distortions hinder complete spin alignment even at low temperatures.

Overall, the heat capacity data reinforce the presence of a magnetically frustrated state in $Ba_3Sb_{1+x}Co_{2-x}O_{9-\delta}$, characterized by broad spin freezing and persistent short-range correlations.

D. AC susceptibility

To investigate the dynamical nature of the spin-glass state in $Ba_3Sb_{1+x}Co_{2-x}O_{9-\delta}$, we performed AC susceptibility measurements as a function of frequency (1–1000 Hz) and temperature (2–50 K). The sample was cooled to 2 K before applying a small AC magnetic field of 10 Oe to assess its temperature-dependent response. The real part of the AC susceptibility, recorded between 24 K and 36 K, is presented in Fig. 5. A broad peak appears near 28.3 K for $\nu = 1$ Hz, and this peak systematically shifts to higher temperatures with increasing frequency. The peak positions determined for various frequencies are listed in Table III. These temperatures were extracted from the minima of the first susceptibility derivative with respect to temperature. The frequency-dependent shift in peak position indicates a delay in spin relaxation, characteristic of a glassy magnetic state. Additionally, the gradual reduction in peak height with increasing frequency is a well-known signature of spin-glass behavior.

To quantify the frequency dependence of the freezing temperature, we employed the Mydosh parameter S, which characterizes the relative shift in peak position with frequency and serves as a diagnostic tool for distinguishing different types of spin-glass systems [47,48]:

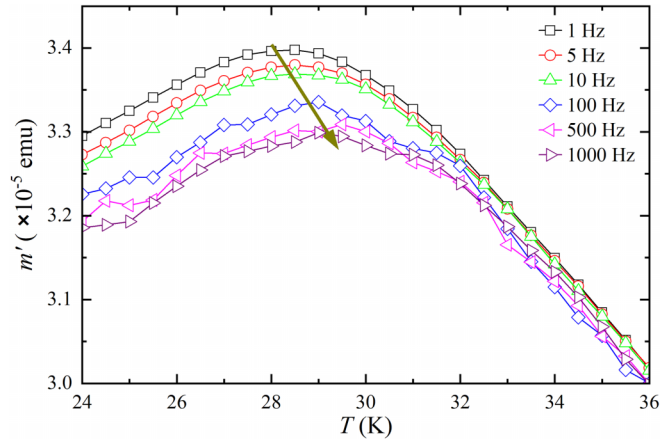


FIG. 5. Temperature dependence of the real part of the AC magnetization measured at various frequencies.

$$S = \frac{\Delta T_f}{T_f \Delta \log_{10}(\nu)}, \tag{7}$$

where $\Delta \log_{10}(\nu) = \log_{10}(\nu_2) - \log_{10}(\nu_1)$ and $\Delta T_f = (T_f)_{\nu_2} - (T_f)_{\nu_1}$. For canonical spin glasses, S typically falls within the range of 0.005–0.01, whereas in cluster-glass systems, it varies between 0.01 and 0.05 [49]. Our analysis yields an average S value of 0.016 ± 0.003, consistent with a cluster-glass system [50].

We applied different theoretical models to the AC susceptibility data to further analyze the glassy dynamics. The critical slowing down of spin relaxation can be described using the power-law scaling equation [4,49,51]:

$$\tau = \tau_0 \left(\frac{T_f - T_g}{T_g} \right)^{-z\nu'}, \tag{8}$$

where τ represents the characteristic relaxation time corresponding to the frequency ν, T_g is the freezing temperature in the $\nu \to 0$ limit, τ_0 is the spin-flip time of an individual spin or cluster, and $z\nu'$ is the critical exponent related to the correlation length. This equation is often rewritten as

$$\log_{10} \nu = \log_{10} \nu_0 + z\nu' \log_{10} \left(\frac{T_f - T_g}{T_g} \right), \tag{9}$$

where $\nu = 2\pi/\tau$. As depicted in Fig. 6(a), the plot of $\log_{10} \nu$ versus $\log_{10}(T_f/T_g - 1)$ follows a linear trend. With T_g fixed at 28 K, the power-law fit yields $z\nu' = 3.95$ and $\tau_0 = 1.12 \times 10^{-7}$ s. These values are consistent with a cluster-glass system, as canonical spin glasses typically exhibit $z\nu'$ in the range

TABLE III. Peak temperature as a function of frequency.

Frequency (Hz)	Peak Temperature (K)
5	28.4
10	28.5
100	29.0
500	29.4
1000	29.5

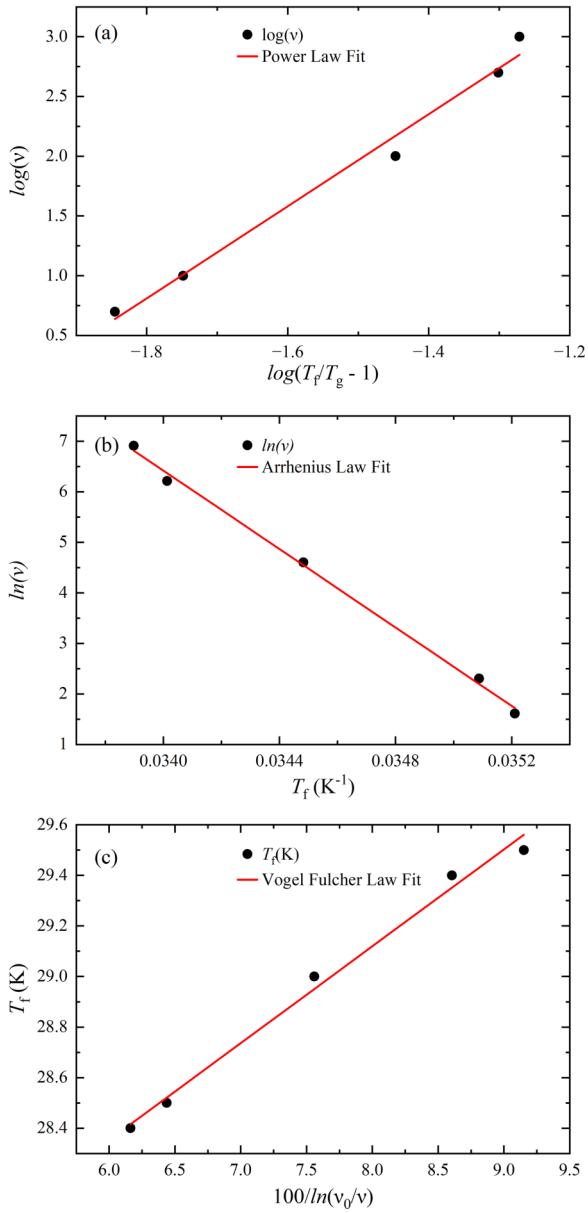


FIG. 6. Fitting of the frequency dependence of the freezing temperature using (a) the power law, (b) the Arrhenius law, and (c) the Vogel-Fulcher law.

of 10–12 and τ_0 around 10^{-12} to 10^{-13} s, whereas cluster glasses generally show $z\nu'$ between 4 and 6 and τ_0 in the range of 10^{-7} to 10^{-9} s [52,53].

We also examined the Arrhenius law, which describes systems with weakly interacting spins [4]:

$$\tau = \tau^* \exp\left(\frac{E_a}{k_B T_f}\right), \tag{10}$$

where E_a/k_B represents the activation energy of the relaxation barriers. The fit, shown in Fig. 6(b), results in an unphysically small $\tau^* = 5.12 \times 10^{-60}$ s and an unrealistically large $E_a/k_B = 3880.57$ K. These findings confirm that the Arrhenius model is unsuitable for our system, likely due to the presence of interacting magnetic clusters rather than isolated spin entities.

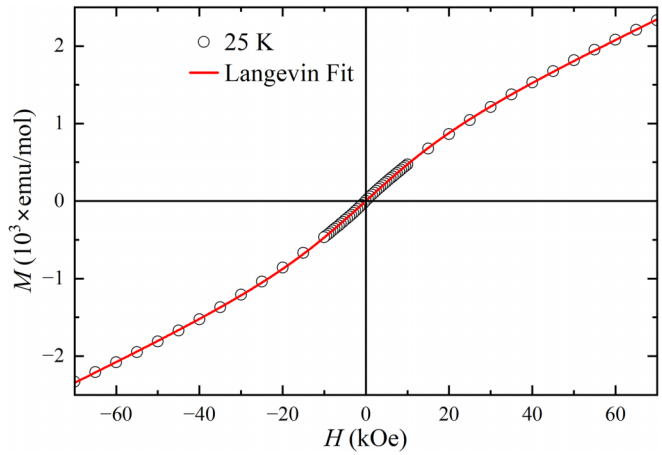


FIG. 7. Estimation of the cluster size using the Langevin function.

Finally, we applied the Vogel-Fulcher law, which accounts for interactions among clusters [49,53]:

$$\tau = \tau_0 \exp\left(\frac{E_a}{k_B(T_f - T_0)}\right), \tag{11}$$

where T_0 represents the interaction strength among magnetic entities. The corresponding linear fit in Fig. 6(c) yields $E_a/k_B = 38.30$ K and $T_0 = 26.05$ K. The nonzero T_0 indicates the presence of interacting clusters, further supporting the cluster-glass interpretation.

The interaction strength can also be assessed using the Tholence criterion [52,54]:

$$\delta T_{Th} = \frac{T_f - T_0}{T_0}. \tag{12}$$

For $Ba_3Sb_{1+x}Co_{2-x}O_{9-\delta}$, we obtain $\delta T_{Th} = 0.11$, consistent with values reported for other cluster-glass systems [55,56]. These findings collectively establish $Ba_3Sb_{1+x}Co_{2-x}O_{9-\delta}$ as a cluster glass with significant antisite disorder, distinguishing it from conventional spin-glass systems.

E. Estimation of cluster size

The characteristic size of magnetic clusters in $Ba_3Sb_{1+x}Co_{2-x}O_{9-\delta}$ can be estimated by fitting the isothermal magnetization data to the Langevin function, which describes the behavior of paramagnetic or superparamagnetic entities. The Langevin equation is given by [57]

$$M(H) = N\mu\left[\coth\left(\frac{\mu H}{k_B T}\right) - \frac{k_B T}{\mu H}\right] + \chi H, \tag{13}$$

where N is the number of magnetic clusters per mole, μ is the magnetic moment per cluster (in μ_B), and χ represents a field-independent Curie-type contribution arising from noninteracting spins [58]. At low magnetic fields, the first term dominates due to cluster magnetization saturation, whereas at high fields, the linear χH term becomes significant. The isothermal magnetization data at 25 K were fitted using Eq. (13), as shown in Fig. 7.

To estimate the cluster size, we first determine N from the fitting parameters $N\mu$ and $\mu/k_B T$. Assuming a spherical

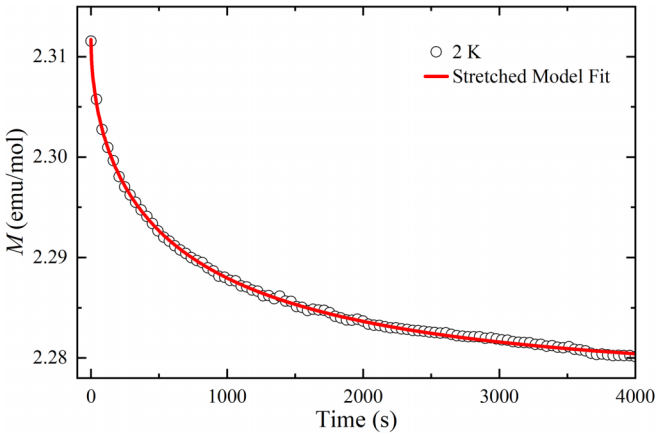


FIG. 8. Time-dependent relaxation of field-cooled magnetization after a waiting time of $t = 100$ s.

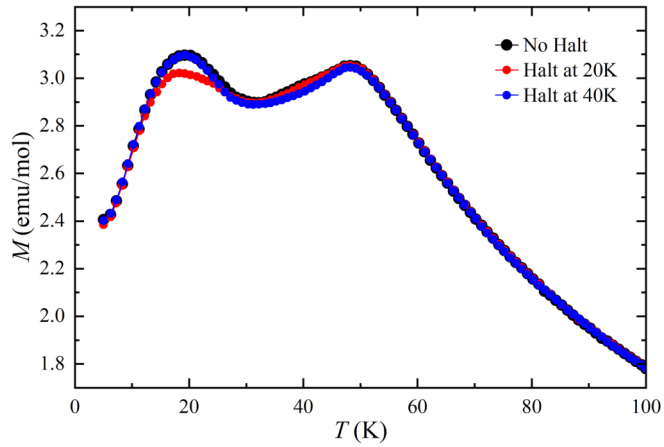


FIG. 9. DC magnetization measured with and without halts at two different temperatures ($T = 20$ and 40 K).

cluster geometry, the cluster volume can be expressed as $V = \frac{4}{3}\pi R^3$, where R is the average cluster radius. Additionally, the volume can be related to the sample density ρ as $V = M/\rho$.

Equating these two expressions, the cluster radius is given by

$$R = \left(\frac{3M}{4\pi\rho N}\right)^{1/3}. \tag{14}$$

From the fitted parameters, we obtain $N = 19.0235 \times 10^{24}$, leading to an estimated average cluster size of $R \approx 1.68$ nm. This value is consistent with those reported for other cluster-glass systems, further supporting the presence of magnetically interacting clusters in $Ba_3Sb_{1+x}Co_{2-x}O_{9-\delta}$ [59].

F. Nonequilibrium dynamics

1. Thermoremanent magnetization

Observing magnetic relaxation below the freezing temperature is another hallmark of spin-glass behavior [55,60]. To investigate the thermoremanent magnetization, the sample was cooled to a temperature well below the spin-glass transition temperature following the field-cooled protocol. The sample was cooled to 2 K in a weak applied magnetic field of 100 Oe. Upon reaching 2 K, the field was removed, and after a waiting time of 100 s, the time evolution of magnetization was recorded for 4000 s, as shown in Fig. 8. The magnetization exhibits a characteristic nonequilibrium relaxation, following an exponential decay with time, a signature of spin-glass dynamics.

The time-dependent magnetization data were analyzed using the well-established stretched exponential model [61], given by

$$m(t) = m_0 - m_g \exp\left[-\left(\frac{t}{\tau}\right)^{\beta}\right], \tag{15}$$

where m_0 represents the static component of the magnetization, m_g is the glassy magnetization component, τ is the mean relaxation time, and β is the stretching exponent. Although this model lacks a rigorous theoretical foundation, it has been widely used to characterize magnetic relaxation phenomena in spin-glass systems [62].

For a spin glass, β typically lies between 0 and 1. A value of $\beta = 0$ implies no relaxation, whereas $\beta = 1$ corresponds to a purely exponential relaxation process [49]. The stretching exponent thus provides insight into the distribution of relaxation times within the system. The best-fit parameters obtained from the analysis are $m_0 = 2.277$ emu/mol or 6.957×10^{-5} emu, $\tau = 704$ s, and $\beta = 0.548$. The nonzero values of these parameters confirm the presence of a magnetically frustrated phase [56,63,64]. Furthermore, the stretched exponential behavior suggests that the system evolves through a complex energy landscape consisting of multiple metastable states [65,66].

2. Magnetic memory effect

To probe the low-temperature magnetic dynamics further, we performed a magnetic memory measurement using the zero-field-cooled protocol [60]. In this experiment, the sample was first cooled from room temperature to the target temperature at a constant rate of 3 K/min and then held (halted) at that temperature for 2 hours. Following this dwell period, the sample was cooled further to 2 K. Magnetization was then recorded during the warming cycle under an applied magnetic field of 100 Oe. For comparison, a reference measurement (referred to as the "no-halt" curve) was carried out by cooling the sample continuously from room temperature down to 2 K at the same rate without any intermediate halts.

Two halt temperatures were selected: 40 K and 20 K. The results are shown in Fig. 9. For the halt at 40 K, the magnetization curve displays a weak shoulder near the halt temperature, while for the 20 K halt, a distinct dip is observed at 20 K in the warming curve. These features indicate that the system retains a memory of the thermal history, suggesting the presence of a metastable glassy magnetic state below the irreversible temperature.

The observed memory effect can be understood within the framework of spin-glass physics, where the energy landscape is characterized by many valleys separated by barriers of varying heights [67]. At a given temperature T_i, relaxation processes are governed by thermally activated transitions over energy barriers comparable to the thermal energy $k_B T_i$. While higher-energy barriers remain inaccessible, relaxation through

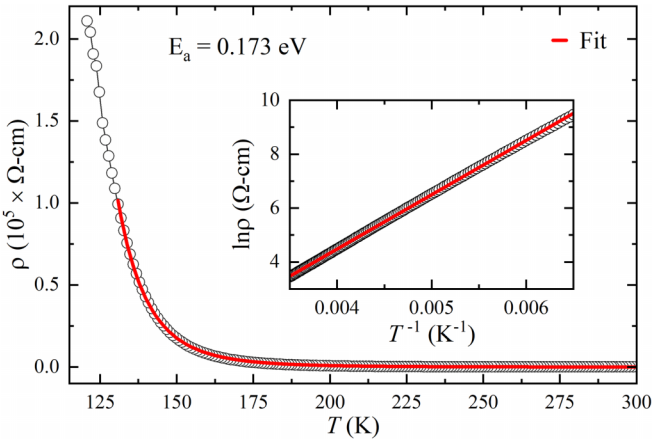


FIG. 10. Temperature-dependent DC resistivity of $Ba_3Sb_{1+x}Co_{2-x}O_{9-\delta}$ in zero applied magnetic field. The main panel shows the resistivity (ρ) plotted as a function of temperature (120–300 K), while the inset presents the Arrhenius fit in the form of ln ρ vs T^{-1}.

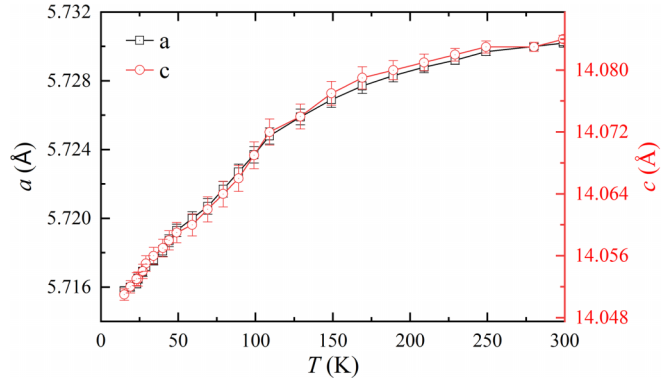


FIG. 11. Temperature dependence of the lattice parameters a and c for $Ba_3Sb_{1+x}Co_{2-x}O_{9-\delta}$. Both parameters show a gradual decrease with cooling, indicating thermal contraction without any structural phase transition.

lower-energy barriers proceeds efficiently, leading to a redistribution of the system into deeper energy minima.

Upon further cooling, relaxation mechanisms at lower-energy scales dominate, largely independent of the previous equilibration at T_i. However, when the system is reheated, the previously equilibrated energy barriers at k_BT_i become reactivated, leading to a slowdown in the relaxation process. This manifests as memory dips in the magnetization curve, confirming that the system retains a record of its thermal history. Such behavior is a defining characteristic of spin glasses, highlighting the presence of a rugged energy landscape with a hierarchy of metastable states.

G. Electrical resistivity

Figure 10 presents the temperature-dependent resistivity (ρ) measured in zero magnetic fields from 120 to 300 K. Below 120 K, the resistivity exceeds the measurable range of our PPMS system, indicating a highly insulating behavior at low temperatures. The resistivity data in the measured temperature range exhibit an activated behavior, well described by the Arrhenius relation:

$$\rho(T) = \rho_0 \exp\left(\frac{E_a}{k_BT}\right), \tag{16}$$

where E_a is the activation energy, ρ_0 is a prefactor, and k_B is the Boltzmann constant. A linear fit to the ln ρ versus T^{-1} plot (inset of Fig. 10) yields $E_a = 1791 \pm 4$ K (∼0.173 eV) and $\rho_0 = 0.115 \pm 0.004$ Ω cm, confirming thermally activated transport.

The observed activated transport behavior suggests that $Ba_3Sb_{1+x}Co_{2-x}O_{9-\delta}$ is a band insulator or a polaronic semiconductor. The extracted activation energy (∼0.173 eV) is comparable to the band gap of narrow-gap semiconductors or the small-polaron hopping energy observed in transition-metal oxides [68,69]. The absence of a successful fit with the Mott variable-range hopping (VRH) model [70] implies that the conduction mechanism is not dominated by hopping between localized states near the Fermi level, ruling out strong disorder-induced localization.

The large resistivity at lower temperatures and the failure of the VRH model suggest that charge transport is likely governed by intrinsic bandlike conduction rather than disorder-driven hopping. This behavior is consistent with insulating oxides containing Co^{3+}, where the electronic gap arises from the crystal-field splitting of d orbitals and the strong on-site Coulomb interaction (U) [71]. Face-sharing CoO_6 octahedral dimers in $Ba_3Sb_{1+x}Co_{2-x}O_{9-\delta}$ may also contribute to the insulating nature, as direct Co-Co interactions could lead to an electronic band structure with a significant gap.

H. Temperature-dependent x-ray diffraction

We performed temperature-dependent x-ray diffraction measurements on $Ba_3Sb_{1+x}Co_{2-x}O_{9-\delta}$ to investigate possible structural changes associated with the magnetic transitions. The evolution of the lattice parameters, a and c, was tracked from 300 K down to 15 K, as shown in Fig. 11. The extracted lattice parameters are in good agreement with those obtained from our neutron powder diffraction data.

Our analysis reveals a smooth, monotonic decrease in both lattice constants with decreasing temperature, consistent with typical thermal contraction driven by anharmonic lattice vibrations. Importantly, no anomalies or discontinuities are observed in the lattice parameters, indicating the absence of any structural phase transition in the investigated temperature range.

The lack of structural distortions suggests that the observed spin-glass behavior in the magnetic measurements is not associated with a symmetry-lowering structural transition. Instead, the spin-glass state likely originates from intrinsic magnetic interactions, such as frustration arising from the face-sharing CoO_6 octahedral dimers or disorder effects due to Sb/Co site mixing. The absence of a structural anomaly further implies that the observed low-temperature magnetic dynamics are governed primarily by electronic and magnetic degrees of freedom rather than lattice distortions.

IV. DISCUSSION

The comprehensive set of measurements—including DC and AC magnetization, heat capacity, magnetic memory and aging, electrical resistivity, temperature-dependent x-ray diffraction, and neutron powder diffraction—collectively establish that $Ba_3Sb_{1+x}Co_{2-x}O_{9-\delta}$ does not exhibit long-range magnetic order down to 1.5 K. Instead, it enters a frozen magnetic state consistent with a cluster spin glass. Central to this behavior is the underlying crystal structure, which promotes disorder and magnetic frustration.

Structurally, $Ba_3Sb_{1+x}Co_{2-x}O_{9-\delta}$ crystallizes in a 6H-hexagonal perovskite structure featuring face-sharing CoO_6 octahedral dimers. Each unit cell contains two crystallographically equivalent Co-Co dimers, with an intradimer Co-Co distance of approximately 2.64 Å and the shortest interdimer distance around 5.73 Å. The combination of these compact Co-Co dimers, significant intersite disorder between Co and Sb ions ($\sim 30\%$), and notable oxygen nonstoichiometry ($\delta \sim 0.54$) introduces strong spatial variations in local magnetic exchange pathways. This structural disorder frustrates coherent long-range magnetic interactions and facilitates the formation of magnetically correlated clusters with short-range interactions.

We expect that the Co-Co dimers exhibit predominant antiferromagnetic coupling within the dimers, due to direct exchange and orbital overlap effects inherent to face-sharing geometry. In contrast, the relatively larger interdimer distances and the observed positive Curie-Weiss temperature ($\theta \sim 21$ K) suggest net ferromagnetic interactions between dimers within the *ab* plane. Similar magnetic motifs—antiferromagnetic intracluster coupling coexisting with ferromagnetic intercluster interactions—have been reported in other hexagonal perovskite systems, such as $Ba_4NbMn_3O_{12}$ [41]. This hierarchy of interactions—dimer-level antiferromagnetic and cluster-level ferromagnetic coupling—leads to a frustrated network of interacting clusters that collectively freeze into a glassy magnetic state.

DC magnetization data reveal a clear bifurcation between zero-field-cooled and field-cooled curves at low temperatures, characteristic of spin-glass behavior. The high-temperature susceptibility follows a Curie-Weiss law, and the derived effective moment is consistent with a mixed-valence scenario for cobalt. Based on structural analysis and bond-valence considerations, we estimate that the Co ions adopt an average valence of +2.9, corresponding to a mixture of roughly 10 % Co^{2+} and 90 % Co^{3+}. While our working model assumes high-spin Co^{2+} and intermediate-spin Co^{3+} states, we stress that these assignments remain tentative due to the sensitivity of cobalt spin states to local structural environments. In systems such as $LaCoO_3$ [34,35,72], even minor structural distortions are known to stabilize intermediate-spin states, and similar effects may be active in $Ba_3Sb_{1+x}Co_{2-x}O_{9-\delta}$.

AC susceptibility data exhibit a frequency-dependent shift in the freezing temperature, and the dynamics are best described by the Vogel-Fulcher model. This points to a collective spin-freezing process involving weakly interacting spin clusters, rather than independent paramagnetic spins. Magnetization isotherms further support this interpretation: Their nonlinearity at low temperatures and the extracted effective moment from Langevin fitting are consistent with the presence of correlated spin clusters.

The nonequilibrium nature of the magnetic state is corroborated by thermoremanent magnetization and magnetic memory experiments, which display pronounced aging effects and history dependence—key signatures of spin-glass dynamics. Heat capacity data also align with this picture, showing no sharp anomalies indicative of magnetic ordering but instead a broad hump at low temperatures, likely arising from short-range spin correlations and low-energy excitations.

Temperature-dependent XRD and neutron powder diffraction confirm that no structural phase transition occurs across the magnetic transition. The continuous lattice contraction and unchanged space group symmetry support the conclusion that the spin freezing is driven not by a structural instability but by intrinsic frustration and disorder. Neutron diffraction further reveals no long-range magnetic order or significant diffuse scattering, implying that the correlation length of magnetic clusters is short and the signal is buried in the background.

Finally, electrical resistivity measurements show semiconducting behavior with Arrhenius-type activation and no evidence for variable-range hopping, implying thermally activated transport and further underscoring the role of disorder in both electronic and magnetic properties.

In summary, the structural framework of $Ba_3Sb_{1+x}Co_{2-x}O_{9-\delta}$—characterized by face-sharing CoO_6 dimers, substantial cation disorder, and oxygen vacancies—plays a pivotal role in promoting frustrated interactions and cluster formation. These features culminate in a cluster spin-glass ground state with slow dynamics and emergent magnetic memory effects. Future studies using local probes such as muon spin relaxation (μSR) or inelastic neutron scattering will be instrumental in revealing the microscopic origin of these correlated clusters and their low-energy excitations.

V. CONCLUSION

Our comprehensive study of $Ba_3Sb_{1+x}Co_{2-x}O_{9-\delta}$ reveals a low-temperature state devoid of long-range magnetic order. DC and AC susceptibility measurements point to a spin-freezing transition with Vogel-Fulcher dynamics. At the same time, Langevin fits of the isothermal magnetization indicate the formation of finite-sized, interacting spin clusters. Complementary thermoremanent magnetization and memory effect experiments reinforce a spin-glass-like state. Heat capacity and neutron diffraction data show no sharp anomalies or magnetic Bragg peaks down to 1.5 K. Rietveld refinements underscore significant Co/Sb intersite disorder and oxygen vacancies, likely introducing exchange randomness and magnetic frustration. Additionally, our findings further support the semiconducting behavior observed via an Arrhenius-type resistivity and the absence of structural transitions from temperature-dependent XRD.

These results establish $Ba_3Sb_{1+x}Co_{2-x}O_{9-\delta}$ as a promising cluster spin-glass candidate in which intrinsic disorder and frustration suppress conventional magnetic order. The exotic spin state of Co in face-sharing hexagonal perovskites thus emerges as an intriguing platform for future studies. Probing this state with advanced local and spectroscopic techniques

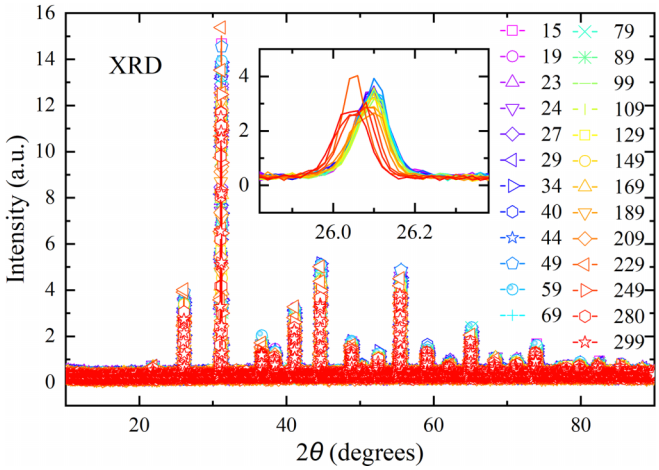


FIG. 12. Temperature-dependent x-ray diffraction patterns of $Ba_3Sb_{1+x}Co_{2-x}O_{9-\delta}$ measured from 15 K to 300 K. The inset shows an enlarged view of a selected peak, highlighting the shift in peak position with temperature.

may unveil novel quantum phenomena and inspire innovative approaches to tailor spin dynamics in complex oxide systems. Future studies on related hexagonal perovskites with controlled Co/Sb ordering or alternative dimer-forming ions (e.g., Rh, Ir, or Ru) may offer further insight into how structural motifs and disorder levels govern the emergence of glassy versus quantum-disordered ground states.

ACKNOWLEDGMENTS

We gratefully acknowledge Eva Brücher for her valuable assistance with magnetization, heat capacity, and resistivity measurements using the Quantum Design MPMS-XL and PPMS systems at the Max Planck Institute for Solid State Research. We also thank R. Rae and C. Kirk for their support with the x-ray diffraction measurements at the University of Edinburgh, UK. We are further indebted to C. Stock (School of Physics and Astronomy, University of Edinburgh) for insightful and stimulating discussions.

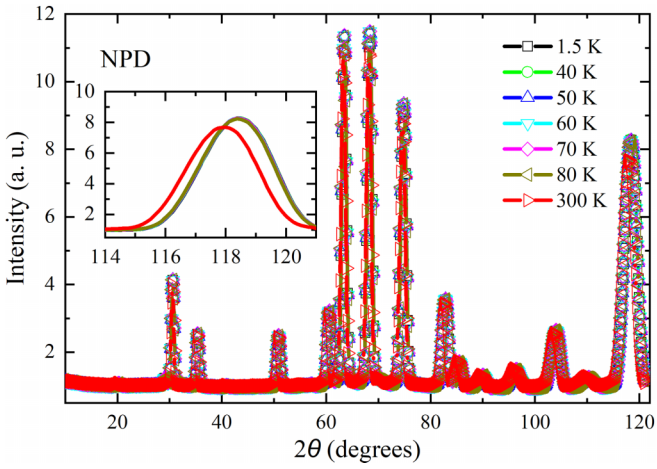


FIG. 13. Temperature-dependent neutron powder diffraction patterns of $Ba_3Sb_{1+x}Co_{2-x}O_{9-\delta}$ measured from 1.5 K to 300 K. No additional reflections appear at low temperatures, confirming the absence of magnetic transitions. The inset presents an enlarged view of a selected peak to illustrate the temperature-dependent shift in peak position.

TABLE IV. Bond valence sum calculations for $Ba_3Sb_{1+x}Co_{2-x}O_{9-\delta}$ at room temperature, extracted from Rietveld refinement of neutron diffraction data collected at room temperature. The BVS values were determined using the EXPO version 2.3.5 software to estimate the effective charge on each atom based on the assumed valence states. CN denotes the coordination number.

Atom	CN	Valence Assumed	BVS
Ba1	12	+2	2.254
Ba2	12	+2	2.175
Co1	6	+3	2.313
Sb2	6	+5	4.822
Sb1	6	+5	4.496
Co2	6	+3	2.074
O1	8	−2	1.878
O2	8	−2	1.874

DATA AVAILABILITY

The data that support the findings of this article are openly available [73]; embargo periods may apply.

APPENDIX A: TEMPERATURE-DEPENDENT XRD AND NPD

To investigate the structural stability of $Ba_3Sb_{1+x}Co_{2-x}O_{9-\delta}$ as a function of temperature, we performed temperature-dependent x-ray diffraction and neutron powder diffraction measurements from 1.5 K to 300 K. The XRD and NPD patterns exhibit no additional diffraction peaks at low temperatures, indicating the absence of structural and magnetic phase transitions. Instead, a systematic shift in peak positions with decreasing temperature suggests thermal contraction of the lattice. The insets of Figs. 12 and 13 highlight an enlarged view of a representative diffraction peak, illustrating this shift in more detail.

APPENDIX B: BOND VALENCE SUM

The bond valence sum analysis, performed using EXPO version 2.3.5 [74] on neutron diffraction data, provides insights into the local bonding environment and charge distribution within $Ba_3Sb_{1+x}Co_{2-x}O_{9-\delta}$. Table IV shows that the BVS values for Ba atoms are close to the expected +2 valence, while those for Sb atoms are slightly below the ideal +5, suggesting minor structural distortions or covalency effects. The Co sites exhibit deviations from the assumed +3 valence, with Co1 showing an underbonded state (2.313) and Co2 being closer to +2 (2.074), supporting the presence of mixed-valence Co^{2+}/Co^{3+} states inferred from magnetic measurements. The oxygen atoms display BVS values slightly below the ideal −2, consistent with oxygen nonstoichiometry observed in the refinement. These results

highlight the interplay between cation disorder, oxygen vacancies, and the complex charge distribution, which likely contribute to the unconventional magnetic behavior of the compound.

[1] L. Balents, Spin liquids in frustrated magnets, Nature (London) **464**, 199 (2010).

[2] C. Broholm, R. J. Cava, S. A. Kivelson, D. G. Nocera, M. R. Norman, and T. Senthil, Quantum spin liquids, Science **367**, eaay0668 (2020).

[3] R. Moessner and A. P. Ramirez, Geometrical frustration, Phys. Today **59**(2), 24 (2006).

[4] K. Binder and A. P. Young, Spin glasses: Experimental facts, theoretical concepts, and open questions, Rev. Mod. Phys. **58**, 801 (1986).

[5] K. Binder and W. Kob, *Glassy Materials and Disordered Solids* (World Scientific, Singapore, 2005).

[6] V. M. Katukuri, S. Nishimoto, I. Rousochatzakis, H. Stoll, J. van den Brink, and L. Hozoi, Strong magnetic frustration and anti-site disorder causing spin-glass behavior in honeycomb Li_2RhO_3, Sci. Rep. **5**, 14718 (2015).

[7] R. C. Sahoo, S. Das, and T. K. Nath, Influence of magnetic frustration and structural disorder on magnetocaloric effect and magneto-transport properties in $La_{1.5}Ca_{0.5}CoMnO_6$ double perovskite, J. Appl. Phys. **123**, 013902 (2018).

[8] C. A. Bridges, T. Hansen, A. S. Wills, G. M. Luke, and J. E. Greedan, Frustrated magnetism and the effects of titanium substitution in the mixed-valence oxide $BaV_{10-x}Ti_xO_{15}$, Phys. Rev. B **74**, 024426 (2006).

[9] L. T. Nguyen and R. J. Cava, Hexagonal perovskites as quantum materials, Chem. Rev. **121**, 2935 (2021).

[10] L. T. Nguyen and R. J. Cava, Trimer-based spin liquid candidate $Ba_4NbIr_3O_{12}$, Phys. Rev. Mater. **3**, 014412 (2019).

[11] A. Bandyopadhyay, S. Lee, D. T. Adroja, G. B. G. Stenning, A. Berlie, M. R. Lees, R. A. Saha, D. Takegami, A. Meléndez-Sans, G. Poelchen, M. Yoshimura, K. D. Tsuei, Z. Hu, C.-W. Kao, Y.-C. Huang, T.-S. Chan, and K.-Y. Choi, Quantum spin liquid ground state in the trimer rhodate $Ba_4NbRh_3O_{12}$, Phys. Rev. B **109**, 184403 (2024).

[12] A. Ali, H.-S. Kim, P. Yadav, S. Lee, D. Yoon, and S. Choi, Partial molecular orbitals in face-sharing $3d$ manganese trimer: Comparative studies on $Ba_4TaMn_3O_{12}$ and $Ba_4NbMn_3O_{12}$, Phys. Rev. Res. **6**, 013231 (2024).

[13] J. A. Quilliam, F. Bert, A. Manseau, C. Darie, C. Guillot-Deudon, C. Payen, C. Baines, A. Amato, and P. Mendels, Gapless quantum spin liquid ground state in the spin-1 antiferromagnet 6H-$Ba_3NiSb_2O_9$, Phys. Rev. B **93**, 214432 (2016).

[14] H. D. Zhou, E. S. Choi, G. Li, L. Balicas, C. R. Wiebe, Y. Qiu, J. R. D. Copley, and J. S. Gardner, Spin liquid state in the $S = 1/2$ triangular lattice $Ba_3CuSb_2O_9$, Phys. Rev. Lett. **106**, 147204 (2011).

[15] S. Middey, S. Ray, K. Mukherjee, P. L. Paulose, E. V. Sampathkumaran, C. Meneghini, S. D. Kaushik, V. Siruguri, K. Kovnir, and D. D. Sarma, Glasslike ordering and spatial inhomogeneity of magnetic structure in $Ba_3FeRu_2O_9$: Role of Fe/Ru site disorder, Phys. Rev. B **83**, 144419 (2011).

[16] L. Savary and L. Balents, Disorder-induced quantum spin liquid in spin ice pyrochlores, Phys. Rev. Lett. **118**, 087203 (2017).

[17] J.-J. Wen, S. M. Koohpayeh, K. A. Ross, B. A. Trump, T. M. McQueen, K. Kimura, S. Nakatsuji, Y. Qiu, D. M. Pajerowski, J. R. D. Copley, and C. L. Broholm, Disordered route to the Coulomb quantum spin liquid: Random transverse fields on spin ice in $Pr_2Zr_2O_7$, Phys. Rev. Lett. **118**, 107206 (2017).

[18] A. Smerald and F. Mila, Disorder-driven spin-orbital liquid behavior in the $Ba_3XSb_2O_9$ materials, Phys. Rev. Lett. **115**, 147202 (2015).

[19] S. Kundu, A. Hossain, P. K. S., R. Das, M. Baenitz, P. J. Baker, J.-C. Orain, D. C. Joshi, R. Mathieu, P. Mahadevan, S. Pujari, S. Bhattacharjee, A. V. Mahajan, and D. D. Sarma, Signatures of a spin-$\frac{1}{2}$ cooperative paramagnet in the diluted triangular lattice of Y_2CuTiO_6, Phys. Rev. Lett. **125**, 117206 (2020).

[20] S. Kundu, A. Shahee, A. Chakraborty, K. M. Ranjith, B. Koo, J. Sichelschmidt, M. T. F. Telling, P. K. Biswas, M. Baenitz, I. Dasgupta, S. Pujari, and A. V. Mahajan, Gapless quantum spin liquid in the triangular system $Sr_3CuSb_2O_9$, Phys. Rev. Lett. **125**, 267202 (2020).

[21] S.-H. Baek, H. W. Yeo, S.-H. Do, K.-Y. Choi, L. Janssen, M. Vojta, and B. Büchner, Observation of a random singlet state in a diluted Kitaev honeycomb material, Phys. Rev. B **102**, 094407 (2020).

[22] R. Kumar and A. Sundaresan, Antisite disorder driven cluster glass state and colossal magnetoresistance in $MnSb_2Se_4$, Phys. Rev. B **106**, 134423 (2022).

[23] K. Pal and I. Das, Exploring the origin of exchange bias and spin glass behavior in 6H hexagonal perovskite structure: Structural and magnetic analysis, Appl. Mater. Today **39**, 102316 (2024).

[24] V. Petříček, M. Dušek, and L. Palatinus, Crystallographic computing system JANA2006: General features, Z. Kristallogr. - Cryst. Mater. **229**, 345 (2014).

[25] S. Istomin, V. A. Koutcenko, E. V. Antipov, F. Lindberg, and G. Svensson, Synthesis and characterization of novel 6-H perovskites $Ba_2Co_{2-x}Sb_xO_{6-y}$, $0.6 \leqslant x \leqslant 0.8$ and $x = 1.33$ ($Ba_3CoSb_2O_9$), Mater. Res. Bull. **39**, 1013 (2004).

[26] Y. Doi, Y. Hinatsu, and K. Ohoyama, Structural and magnetic properties of pseudo-two-dimensional triangular antiferromagnets $Ba_3MSb_2O_9$ (M = Mn, Co, and Ni), J. Phys.: Condens. Matter **16**, 8923 (2004).

[27] C. Darie, P. Bordet, M. Viaud, C. Guillot-Deudon, P. Deniard, E. Gautron, C. Colin, F. Porcher, G. Berlanda, F. Bert, P. Mendels, and C. Payen, Two new cubic perovskite oxides $Ba_3CoSb_2O_9$ and $Ba_2SrCoSb_2O_9$: Syntheses, crystal structures and magnetic properties, J. Solid State Chem. **317**, 123701 (2023).

[28] P. Kearins, E. Solana-Madruga, K. Ji, C. Ritter, and J. P. Attfield, Cluster spin glass formation in the double double perovskite $CaMnFeTaO_6$, J. Phys. Chem. C **125**, 9550 (2021).

[29] T. Murakami, M. Avdeev, R. Morikawa, J. R. Hester, and M. Yashima, High proton conductivity in β-Ba_2ScAlO_5 enabled by octahedral and intrinsically oxygen-deficient layers, Adv. Funct. Mater. **33**, 2206777 (2023).

[30] M. I. Gómez, G. Lucotti, J. A. de Morán, P. J. Aymonino, S. Pagola, P. Stephens, and R. E. Carbonio, *Ab initio* structure solution of $BaFeO_{2.8-\delta}$, a new polytype in the system

$BaFeO_y (2.5 \leqslant y \leqslant 3.0)$ prepared from the oxidative thermal decomposition of $BaFe[(CN)_5NO] \cdot 3H_2O$, J. Solid State Chem. **160**, 17 (2001).

[31] D. C. Sinclair, J. M. S. Skakle, F. D. Morrison, R. I. Smith, and T. P. Beales, Structure and electrical properties of oxygen-deficient hexagonal $BaTiO_3$, J. Mater. Chem. **9**, 1327 (1999).

[32] C. de la Calle, J. A. Alonso, A. Aguadero, and M. T. Fernández-Díaz, Phase transformations in $Sr_{0.8}Ba_{0.2}CoO_{2.5}$ brownmillerite: Correlation between structure and transport properties, Dalton Trans. **2009**, 4104 (2009).

[33] S. Mugiraneza and A. M. Hallas, Tutorial: A beginner's guide to interpreting magnetic susceptibility data with the Curie-Weiss law, Commun. Phys. **5**, 95 (2022).

[34] M. A. Korotin, S. Y. Ezhov, I. V. Solovyev, V. I. Anisimov, D. I. Khomskii, and G. A. Sawatzky, Intermediate-spin state and properties of $LaCoO_3$, Phys. Rev. B **54**, 5309 (1996).

[35] G. Maris, Y. Ren, V. Volotchaev, C. Zobel, T. Lorenz, and T. T. M. Palstra, Evidence for orbital ordering in $LaCoO_3$, Phys. Rev. B **67**, 224423 (2003).

[36] N. A. A. M. Amin, S. M. Said, N. M. J. N. Ibrahim, M. M. I. M. Hasnan, M. F. M. Salleh, and A. M. Afifi, Comparative analysis between solution-phase and thin films of cobalt(II) spin crossover (SCO) complexes with 8, 10, 12-carbon alkyl chains based on structural, optical and electrical properties, J. Mater. Sci.: Mater. Electron. **35**, 1930 (2024).

[37] Y.-Y. Chin, H.-J. Lin, Z. Hu, C.-Y. Kuo, D. Mikhailova, J.-M. Lee, S.-C. Haw, S.-A. Chen, W. Schnelle, H. Ishii, N. Hiraoka, Y.-F. Liao, K.-D. Tsuei, A. Tanaka, L. Hao Tjeng, C.-T. Chen, and J.-M. Chen, Relation between the Co-O bond lengths and the spin state of Co in layered cobaltates: A high-pressure study, Sci. Rep. **7**, 3656 (2017).

[38] Y. M. Oey and R. Cava, The effective magnetic moments of Co^{2+} and Co^{3+} in $SrTiO_3$ investigated by temperature-dependent magnetic susceptibility, Mater. Res. Bull. **122**, 110667 (2020).

[39] A. Podlesnyak, M. Russina, A. Furrer, A. Alfonsov, E. Vavilova, V. Kataev, B. Büchner, T. Strässle, E. Pomjakushina, K. Conder, and D. I. Khomskii, Spin-state polarons in lightly-hole-doped $LaCoO_3$, Phys. Rev. Lett. **101**, 247603 (2008).

[40] T. Burnus, Z. Hu, H. H. Hsieh, V. L. J. Joly, P. A. Joy, M. W. Haverkort, H. Wu, A. Tanaka, H.-J. Lin, C. T. Chen, and L. H. Tjeng, Local electronic structure and magnetic properties of $LaMn_{0.5}Co_{0.5}O_3$ studied by x-ray absorption and magnetic circular dichroism spectroscopy, Phys. Rev. B **77**, 125124 (2008).

[41] S. V. Streltsov and D. I. Khomskii, Cluster magnetism of $Ba_4NbMn_3O_{12}$: Localized electrons or molecular orbitals? JETP Lett. **108**, 686 (2018).

[42] L. T. Nguyen, T. Halloran, W. Xie, T. Kong, C. L. Broholm, and R. J. Cava, Geometrically frustrated trimer-based Mott insulator, Phys. Rev. Mater. **2**, 054414 (2018).

[43] G. S. Thakur, S. Chattopadhyay, T. Doert, T. Herrmannsdörfer, and C. Felser, Crystal growth of spin-frustrated $Ba_4Nb_{0.8}Ir_{3.2}O_{12}$: A possible spin liquid material, Cryst. Growth Des. **20**, 2871 (2020).

[44] S. Shibasaki, I. Terasaki, E. Nishibori, H. Sawa, J. Lybeck, H. Yamauchi, and M. Karppinen, Magnetic and transport properties of the spin-state disordered oxide $La_{0.8}Sr_{0.2}Co_{1-x}Rh_xO_{3-\delta}$, Phys. Rev. B **83**, 094405 (2011).

[45] C. Kittel, *Introduction to Solid State Physics* (John Wiley & Sons, 2004).

[46] S. J. Sebastian, K. Somesh, M. Nandi, N. Ahmed, P. Bag, M. Baenitz, B. Koo, J. Sichelschmidt, A. A. Tsirlin, Y. Furukawa, and R. Nath, Quasi-one-dimensional magnetism in the spin-$\frac{1}{2}$ antiferromagnet $BaNa_2Cu(VO_4)_2$, Phys. Rev. B **103**, 064413 (2021).

[47] C. A. M. Mulder, A. J. van Duyneveldt, and J. A. Mydosh, Frequency and field dependence of the ac susceptibility of the AuMn spin-glass, Phys. Rev. B **25**, 515 (1982).

[48] J. Mydosh, Disordered magnetism and spin glasses, J. Magn. Magn. Mater. **157-158**, 606 (1996).

[49] J. A. Mydosh, *Spin Glasses: An Experimental Introduction* (Taylor & Francis, 1993).

[50] P. Bag, P. R. Baral, and R. Nath, Cluster spin-glass behavior and memory effect in $Cr_{0.5}Fe_{0.5}Ga$, Phys. Rev. B **98**, 144436 (2018).

[51] J. Lago, S. J. Blundell, A. Eguia, M. Jansen, and T. Rojo, Three-dimensional Heisenberg spin-glass behavior in $SrFe_{0.90}Co_{0.10}O_{3.0}$, Phys. Rev. B **86**, 064412 (2012).

[52] J. Souletie and J. L. Tholence, Critical slowing down in spin glasses and other glasses: Fulcher versus power law, Phys. Rev. B **32**, 516 (1985).

[53] S. Shtrikman and E. Wohlfarth, The theory of the Vogel-Fulcher law of spin glasses, Phys. Lett. A **85**, 467 (1981).

[54] P. Beauvillain, C. Chappert, J. Renard, and J. Seiden, Critical scaling laws in insulating spin glasses, J. Magn. Magn. Mater. **54-57**, 127 (1986).

[55] R. Mathieu, M. Hudl, and P. Nordblad, Memory and rejuvenation in a spin glass, Europhys. Lett. **90**, 67003 (2010).

[56] R. Kumar, P. Yanda, and A. Sundaresan, Cluster-glass behavior in the two-dimensional triangular lattice Ising-spin compound $Li_2Mn_3O_7$, Phys. Rev. B **103**, 214427 (2021).

[57] G. H. McCabe, T. Fries, M. T. Liu, Y. Shapira, L. R. Ram-Mohan, R. Kershaw, A. Wold, C. Fau, M. Averous, and E. J. McNiff, Bound magnetic polarons in *p*-type $Cu_2Mn_{0.9}Zn_{0.1}SnS_4$, Phys. Rev. B **56**, 6673 (1997).

[58] P. Anil Kumar, A. Nag, R. Mathieu, R. Das, S. Ray, P. Nordblad, A. Hossain, D. Cherian, D. A. Venero, L. DeBeer-Schmitt, O. Karis, and D. D. Sarma, Magnetic polarons and spin-glass behavior in insulating $La_{1-x}Sr_xCoO_3$ ($x = 0.125$ and 0.15), Phys. Rev. Res. **2**, 043344 (2020).

[59] A. Kumar, A. Senyshyn, and D. Pandey, Evidence for cluster spin glass phase with precursor short-range antiferromagnetic correlations in the *B*-site disordered $Ca(Fe_{1/2}Nb_{1/2})O_3$ perovskite, Phys. Rev. B **99**, 214425 (2019).

[60] K. Jonason, E. Vincent, J. Hammann, J. P. Bouchaud, and P. Nordblad, Memory and chaos effects in spin glasses, Phys. Rev. Lett. **81**, 3243 (1998).

[61] R. S. Freitas, L. Ghivelder, F. Damay, F. Dias, and L. F. Cohen, Magnetic relaxation phenomena and cluster glass properties of $La_{0.7-x}Y_xCa_{0.3}MnO_3$ manganites, Phys. Rev. B **64**, 144404 (2001).

[62] R. V. Chamberlin, G. Mozurkewich, and R. Orbach, Time decay of the remanent magnetization in spin-glasses, Phys. Rev. Lett. **52**, 867 (1984).

[63] C. A. Cardoso, F. M. Araujo-Moreira, V. P. S. Awana, E. Takayama-Muromachi, O. F. de Lima, H. Yamauchi, and M.

Karppinen, Spin glass behavior in $RuSr_2Gd_{1.5}Ce_{0.5}Cu_2O_{10-\delta}$, Phys. Rev. B **67**, 020407(R) (2003).

[64] D. Chu, G. G. Kenning, and R. Orbach, Dynamic measurements in a Heisenberg spin glass: CuMn, Phys. Rev. Lett. **72**, 3270 (1994).

[65] A. Bhattacharyya, S. Giri, and S. Majumdar, Spin-glass-like state in GdCu: Role of phase separation and magnetic frustration, Phys. Rev. B **83**, 134427 (2011).

[66] S. Pakhira, C. Mazumdar, R. Ranganathan, S. Giri, and M. Avdeev, Large magnetic cooling power involving frustrated antiferromagnetic spin-glass state in R_2NiSi_3(R = Gd, Er), Phys. Rev. B **94**, 104414 (2016).

[67] H. Mamiya, Universal memory effects in Heisenberg spin glasses and spontaneous restoration of the spin configuration, Phys. Procedia **75**, 711 (2015).

[68] J.-H. Yuan, B. Zhang, Y.-Q. Song, J.-F. Wang, K.-H. Xue, and X.-S. Miao, Planar penta-transition metal phosphide and arsenide as narrow-gap semiconductors with ultrahigh carrier mobility, J. Mater. Sci. **54**, 7035 (2019).

[69] G. Liu, X. Q. Liu, and X. M. Chen, Contribution of oxygen vacancies to the giant dielectric response in $Sm_{1.5}Sr_{0.5}NiO_{4-\delta}$ ceramics, Appl. Phys. A **116**, 1421 (2014).

[70] R. M. Hill, Variable-range hopping, Phys. Status Solidi A **34**, 601 (1976).

[71] J. Chen, X. Wu, and A. Selloni, Electronic structure and bonding properties of cobalt oxide in the spinel structure, Phys. Rev. B **83**, 245204 (2011).

[72] M. W. Haverkort, Z. Hu, J. C. Cezar, T. Burnus, H. Hartmann, M. Reuther, C. Zobel, T. Lorenz, A. Tanaka, N. B. Brookes, H. H. Hsieh, H.-J. Lin, C. T. Chen, and L. H. Tjeng, Spin state transition in $LaCoO_3$ studied using soft x-ray absorption spectroscopy and magnetic circular dichroism, Phys. Rev. Lett. **97**, 176405 (2006).

[73] A. Ali, Raw data for the article entited "Cluster spin glass state in $Ba_3Sb_{1+x}Co_{2-x}O_{9-\delta}$: Cation disorder and mixed-valence Co dimers" [Data set], Zenodo (2025), https://doi.org/10.5281/zenodo.15789706.

[74] A. Altomare, C. Cuocci, C. Giacovazzo, A. Moliterni, R. Rizzi, N. Corriero, and A. Falcicchio, EXPO2013: A kit of tools for phasing crystal structures from powder data, J. Appl. Crystallogr. **46**, 1231 (2013).